IEEE Access
Multidisciplinary : Rapid Review : Open Access Journal

Received 24 April 2023, accepted 26 May 2023, date of publication 5 June 2023, date of current version 12 June 2023.

*Digital Object Identifier 10.1109/ACCESS.2023.3283144*

RESEARCH ARTICLE

# Effect of Electromagnetic Force Caused by PMSM on the Vibration/Noise of Reciprocating Compressors

**CHI-SUNG PARK[1], JAE-HYUN KIM[1], SOO-HWAN PARK[1,2], AND MYUNG-SEOP LIM[1], (Member, IEEE)**

[1]Department of Automotive Engineering, Hanyang University, Seoul 04763, South Korea
[2]Research and Development Division, Hyundai Motor Company, Hwaseong 18280, South Korea

Corresponding author: Myung-Seop Lim (myungseop@hanyang.ac.kr)

This work was supported by the National Research Foundation of Korea (NRF) funded by the Korean Government [Ministry of Science and ICT (MSIT)] under Grant RS-2023-00207865.

**ABSTRACT** The use of pulse width modulation (PWM) to drive permanent magnet synchronous motors (PMSM) inevitably creates current harmonics. The generated current harmonics create harmonic components of the electromagnetic force, causing noise and vibration in the PMSM and affecting the applied system. In this paper, the effect of PMSM's electromagnetic force on noise and vibration of a reciprocating compressor is analyzed. First, two PMSMs with different electromagnetic forces were designed. As the driving method, space vector PWM (SVPWM) was used, and the experimental current waveform was analyzed. Based on the Maxwell stress tensor method, the electromagnetic force of the PMSM was calculated and the noise/vibration characteristics were analyzed. Compressors were manufactured with two PMSMs with different electromagnetic forces and the noise/vibration test results were compared. The electromagnetic force of PMSM affected the noise of the compressor, especially in the domain of twice the carrier frequency, but did not affect the low-order vibrational displacement of the compressor. The finite element analysis method was used, and it was experimentally verified with the manufactured motor and compressor.

**INDEX TERMS** Electromagnetic force density, noise and vibration, permanent magnet synchronous motor (PMSM), pulse width modulation (PWM), reciprocating compressor.

## I. INTRODUCTION

In recent years, with increasing interest in the residential environment, the comfort of sound has become more important. Home appliances, the main cause of indoor noise, are also being actively researched to reduce noise. In the case of a refrigerator, noise/vibration characteristics are important because it is located indoors and operates continuously [1]. And in the refrigeration cycle, the compressor that converts the low-temperature/low-pressure refrigerant into a high-temperature/high-pressure state has a great influence on the noise and vibration of the refrigerator [2]. A motor is used to drive the compressor, and the inverter is mainly used to drive the motor at a variable speed for high efficiency [3], [4], [5], [6]. PMSM is divided into fractional slot concentrated winding (FSCW) and integer slot distributed winding. FSCW with high manufacturability is mainly used in refrigerator compressors. Compared to integer slot distributed winding, FSCW has a lower vibration order, so noise/vibration characteristics are degraded [7], [8], [9]. Therefore, studies on design and control technology of PMSM with FSCW are being actively conducted to reduce noise/vibration. First, factors affecting noise/vibration in PMSM were analyzed, and studies considering the number of poles/slots and current harmonics were also conducted [10], [11], [12], [13], [14], [15], [16]. In addition, noise/vibration caused by asymmetry in the air gap, which may occur due to manufacturing tolerances, was also analyzed [17]. Second, studies on noise/vibration reduction of PMSM drives and electromagnetic noise/vibration in the carrier frequency domain according to DC voltage fluctuations were conducted [18], [19].

The associate editor coordinating the review of this manuscript and approving it for publication was Agustin Leobardo Herrera-May.

This work is licensed under a Creative Commons Attribution-NonCommercial-NoDerivatives 4.0 License.
For more information, see https://creativecommons.org/licenses/by-nc-nd/4.0/

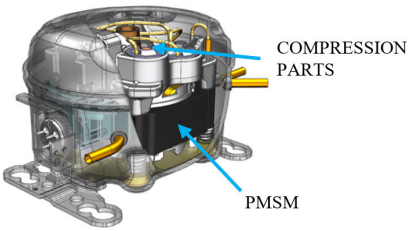


**FIGURE 1.** Structure of the reciprocating compressor.

Also introduces the PWM method and control algorithm for noise/vibration reduction in PMSM [20], [21]. However, no study was conducted on the effect of motor noise/vibration on the noise/vibration of the reciprocating compressor.

Generally, sinusoidal driving mode and square wave driving mode are used for reciprocating compressor. Compared to the square wave driving mode, the sinusoidal driving mode has the advantages of low current harmonics and torque ripple, good starting performance, and flux weakening control [22]. The square wave driving mode has the advantages of simple control algorithm and low switching loss [23]. Here, SVPWM, which is most often used in reciprocating compressors and has good current harmonic characteristics, is analyzed. PWM current is also closely related to noise/vibration characteristics. The PWM current generates an electromotive force in the armature and combines with the permanent magnet (PM) field magnetomotive force to generate an electromagnetic force. Electromagnetic forces are an important factor in causing noise/vibration in PMSM. The structure of the reciprocating compressor is shown in Fig. 1. The PMSM is located under the compression part and is connected by bolts. Because they are structurally connected, the noise/vibration of PMSM affects the noise/vibration of the compressor. In this paper, the characteristics of two PMSMs with different electromagnetic forces were compared and the effect on the noise/vibration of the compressor was analyzed.

## II. NOISE AND VIBRATION OF PMSM

This section analyzes the noise/vibration of two PMSMs designed with different electromagnetic forces. First, the SVPWM current characteristics are analyzed, and the electromagnetic force density is compared. The following compares the noise/vibration of PMSM by experiment and simulation. Here, two-dimensional (2D) and three-dimensional (3D) electromagnetic finite element analysis (FEA) was performed using the commercial software JMAG program.

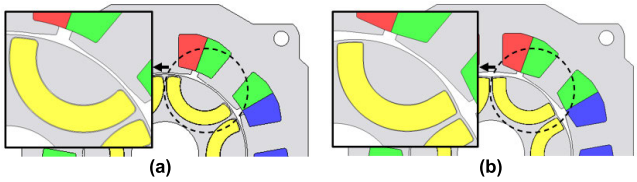


**FIGURE 2.** Configuration of the motor. (a) Model A. (b) Model B.

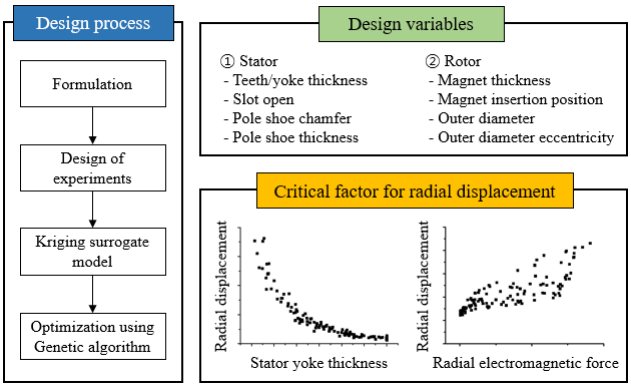


**FIGURE 3.** PMSM design process and critical factor of radial displacement.

**TABLE 1.** Specification of the IPMSM.

| Quantity | Unit | Model A, B |
|---|---|---|
| Number of poles / slots | - | 6 / 9 |
| PM remanence | T | 0.45 |
| Airgap length | mm | 0.6 |
| Stack length | mm | 26 |
| Rated torque | Nm | 0.23 |
| Speed range | Hz | 20 ~75 |
| Winding | - | Concentrated |

### A. DESIGN OF PMSM

In this study, an internal permanent magnet synchronous motor (IPMSM) with high power density and efficiency was used, and Fig. 2 and Table 1 show the configuration and specifications, respectively. Model A in Fig. 2(a) is the base model, and model B in Fig. 2(b) is designed to reduce radial electromagnetic forces compared to the base model. Fig. 3 shows the design process of model B, and nine design variables were selected. The design of experiments (DOE) was implemented as a combination of Optimal Latin hypercube design (OLHD) and sequential maximum distance design (SMDD) [24]. Also, it has a total of 1320 experiment points. By analyzing DOE's 2D FEA results, the critical factors that have the greatest effect on radial displacement were identified as the thickness of the stator yoke and the radial electromagnetic force. Therefore, the thickness of the stator yoke was selected to be the same as that of model A, and optimization was performed to reduce the electromagnetic force in the radial direction. Here, to reduce computation time, a surrogate model was utilized. A surrogate model is a type of functional relationship between input and output variables that serves as an approximation of a complex optimization objective model. In this study, the kriging surrogate model was adopted as a surrogate model, which is widely used in electric motor optimization owing to its high predictability when a non-linear input is used [25]. The kriging surrogate model is defined as follows:

$$\hat{Y}(x) = \boldsymbol{f}(x)^T \hat{\boldsymbol{\beta}} + \boldsymbol{r}(x)^T \boldsymbol{R}^{-1} \left( \boldsymbol{Y} - \boldsymbol{F}\hat{\boldsymbol{\beta}} \right) \tag{1}$$

where, $\boldsymbol{f}(x)$ is the vector of known regression functions, $\hat{\boldsymbol{\beta}}$ is the vector of the unknown regression coefficients, $\boldsymbol{r}(x)$ is the correlation vector between the design points and the prediction points, $\boldsymbol{R}$ is the correlation matrix between the design points, $\boldsymbol{Y}$ is the response matrix of the design points, and $\boldsymbol{F}$ is the vector of the regression function matrix. Then, the optimized model (model B) to reduce radial electromagnetic force was determined using genetic algorithm.

Model A and model B have the same shape and outer dimensions of the stator, the outer diameter of the rotor, and the minimum air gap dimensions. In addition, the radius/thickness of the stator yoke, which has the greatest effect on vibration, is also the same to compare the effect of the electromagnetic force itself on the noise/vibration of PMSM and compressor. On the other hand, the rotor outer diameter shape, PM shape, pole shoe shape and air gap design dimensions are different. The two PMSMs have different electromagnetic forces and are designed to have the same torque constant. Efficiency was analyzed under rated load conditions before comparing the noise/vibration characteristics of model A and model B. Table 2 shows the 2D FEA and dynamo test results of the two models. Here, the load condition, carrier frequency and mechanical angular velocity are 0.23 Nm, 4.5 kHz and 25 Hz, respectively. Model A and model B show similar efficiency. In the next section the measured PWM current is analyzed.

**TABLE 2. Comparison of PMSM efficiency between model A and model B.**

| Item | Quantity | Unit | Model A | Model B |
|---|---|---|---|---|
| 2D FEA | Efficiency | % | 93.41 | 93.46 |
| | Copperloss | W | 1.14 | 1.36 |
| | Coreloss | W | 1.58 | 1.32 |
| Dynamo test | Efficiency | Arms | 93.09 | 93.24 |
| | Copperloss | W | 1.19 | 1.39 |
| | Coreloss | W | 1.67 | 1.39 |

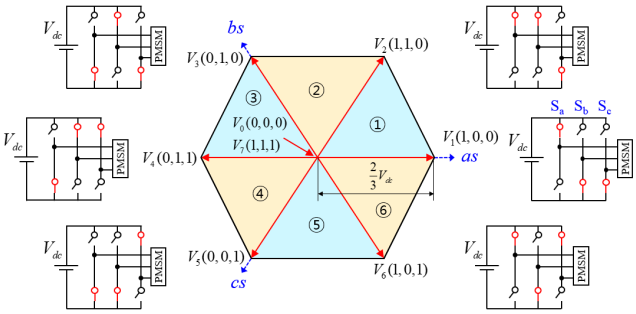


**FIGURE 4. Voltage vector diagram and switching states of SVPWM.**

## B. ANALYSIS OF THE PWM CURRENT

Fig. 4 shows the voltage vector diagram of SVPWM and the switching status of each voltage vector. SVPWM has a total of eight voltage vectors, and each voltage vector has a different switching state. Here, the six voltage vectors $V_1$-$V_6$ are effective voltage vectors that apply effective voltages to the PMSM. The magnitude is the same at $2V_{dc}/3$, only the phase is different. The $V_{dc}$ voltage used is 310V. On the other hand, $V_0$ and $V_7$ cannot apply effective voltage to the PMSM, so they are zero voltage vectors. Fig. 5 shows the switching method and the measured current waveforms for SVPWM. In this study, since noise/vibration according to electromagnetic force is analyzed, the carrier frequency is set to 4.5 kHz for both models. In SVPWM, the placement of the active voltage vector significantly affects the current ripple. It is well known that the current ripple is minimized when the active voltage vector is placed at the center of the half carrier period ($T_s$), as shown in Fig. 5 [26]. Therefore, the frequency of the current ripple would be 9 kHz because the carrier frequency is 4.5 kHz.

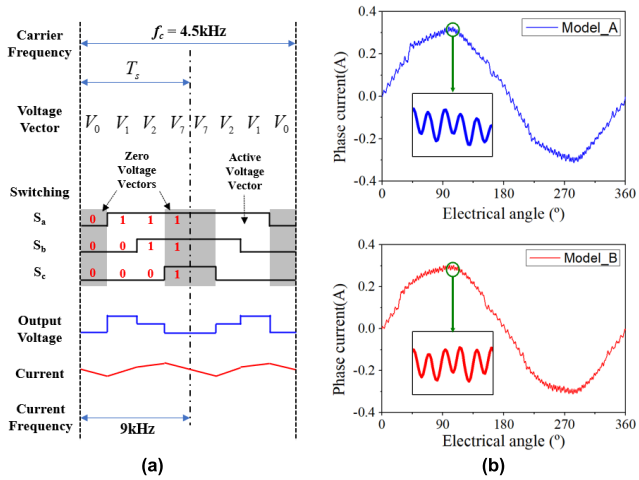


**FIGURE 5. Switching method for SVPWM and measured current waveforms for both models.**

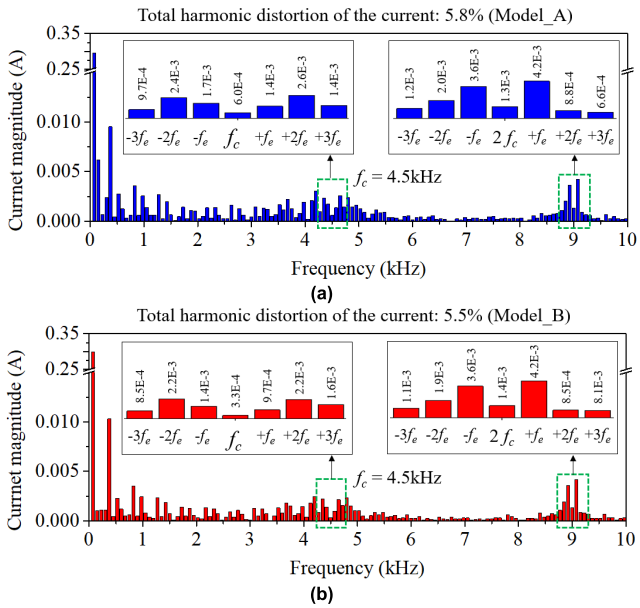


**FIGURE 6. Harmonics analysis of the waveform of the measured current. (a) Model A. (b) Model B.**

Fig. 6 compares the harmonics of the input current through fast Fourier transform (FFT) analysis for two models.

Excluding below 500 Hz, both models have the largest magnitude at 9 kHz, the frequency of the current ripple. The total harmonic distortion (THD) of model A and model B is similar at 5.8% and 5.5%, respectively, and the harmonics are similar even in the $2f_c$ domain. Therefore, the characteristics of the input current generating the armature magnetomotive force are similar in both models.

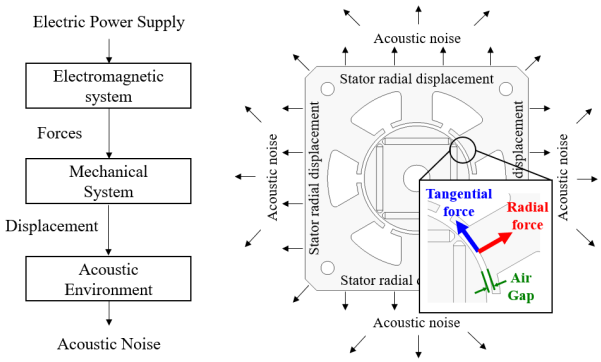


**FIGURE 7.** Mechanisms of vibration and noise generation in PMSM.

### C. ELECTROMAGNETIC FORCE DENSITY

This section compares the radial and tangential electromagnetic force densities for model A and model B. Fig. 7 shows the noise/vibration mechanism of the inner rotor type motor. When power is applied to the motor, electromagnetic force is generated in the radial and tangential directions in the air gap. The generated electromagnetic force flows through the stator and causes the motor to vibrate. Also, the vibration of the motor generates noise, and the noise is radiated into the air.

Electromagnetic forces can be calculated using the Maxwell stress tensor method. First, the radial electromagnetic force density can be calculated as the magnetic flux density of the air gap in the radial and tangential directions, as follows [14], [19].

$$P_r = \frac{B_r^2 - B_t^2}{2\mu_0} \approx \frac{B_r^2}{2\mu_0} \tag{2}$$

Here, $B_r$ and $B_t$ are the radial and tangential airgap magnetic flux densities, respectively, ignoring slot effects. $\mu_0$ is the vacuum permeability. Since the radial airgap magnetic flux density is usually much larger than the tangential airgap magnetic flux density, the radial electromagnetic force density can be approximated using only $B_r$.

The magnetic flux density in the air gap can be expressed as follows by multiplying the sum of the PM field magnetomotive force and the armature magnetomotive force by the relative permeance [10], [19].

$$B = \Lambda_g(F_{PM} + F_{armature}) \tag{3}$$

Here, $\Lambda_g$, $F_{PM}$, and $F_{armature}$ are the relative permeance, the PM field magnetomotive force, and the armature magnetomotive force, respectively, and can be expressed as follows [14], [15].

$$\Lambda_g(\alpha) = \frac{A_0}{2} + \frac{\mu_0}{gk_C}\sum_k A_k \cos(ks\alpha)$$
$$= \Lambda_{g0}\left[1 + \sum_k A_k \cos(ks\alpha)\right] \tag{4}$$

$$F_{PM} = \sum_{\mu=2k\pm1} F_\mu \cos(\mu p\omega_m t - \mu p\alpha + \theta_\mu) \tag{5}$$

$$F_{armature} = \sum_n \sum_\nu F_\nu \cos(np\omega_m t - \nu p\alpha) \tag{6}$$

Here, $\Lambda_{g0}$ is the constant component of the air gap relative permeance, $g$, $A_k$, $s$, and $k$ represent air gap length, harmonic permeance, slot number, integer, respectively. Also, $p$, $\omega_m$, $t$, $\alpha$, and $\theta$ represent pole pair, mechanical angular velocity, time, mechanical angle, phase angle, respectively. $\mu$ is the spatial harmonic order of the PM field, $n$ is time harmonic order of the armature reaction, and $\nu$ is spatial harmonic order of the armature reaction.

By the pole-slot combination, the spatial harmonic order of the armature reaction $\nu$ can be determined as [14].

$$q = \frac{s}{2mp} = \frac{z}{c}, \nu = \frac{2mk}{c} + 1 \tag{7}$$

where, $q$ is the number of slots per phase per pole, $m$ is the number of phases, and $c$ and $z$ are relatively prime numbers. Therefore, the radial electromagnetic force density can be derived using (2)-(7).

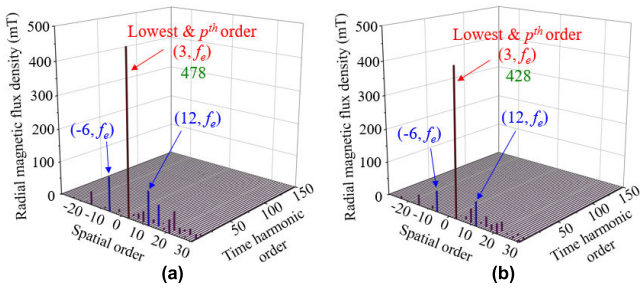


**FIGURE 8.** Radial magnetic flux density in air gap due to relative permeance and PM field magnetomotive force. (a) Model A. (b) Model B.

Fig. 8 shows the 2D FFT results of the radial magnetic flux density in the air gap due to PM field magnetomotive force and relative permeance. Compared to model A, model B has a lower radial magnetic flux density due to a longer average air gap length and rotor design differences. Since the pole pair is 3, the spatial harmonic order of the radial magnetic flux density is 3rd order at the fundamental electrical angular velocity $f_e$. The spatial order of the radial magnetic flux density 3rd is the lowest order and the largest in magnitude.

Fig. 9 shows the 2D FFT results of the radial magnetic flux density in the air gap due to armature magnetomotive force and relative permeance. The 2D electromagnetic FEA used the measured PWM current shown in Fig. 5. The load condition, carrier frequency, and electrical angular velocity are 0.23 Nm, 4.5 kHz, and 75 Hz, respectively. Therefore, the time harmonics are 60th order for $f_c$ and 120th order for $2f_c$.

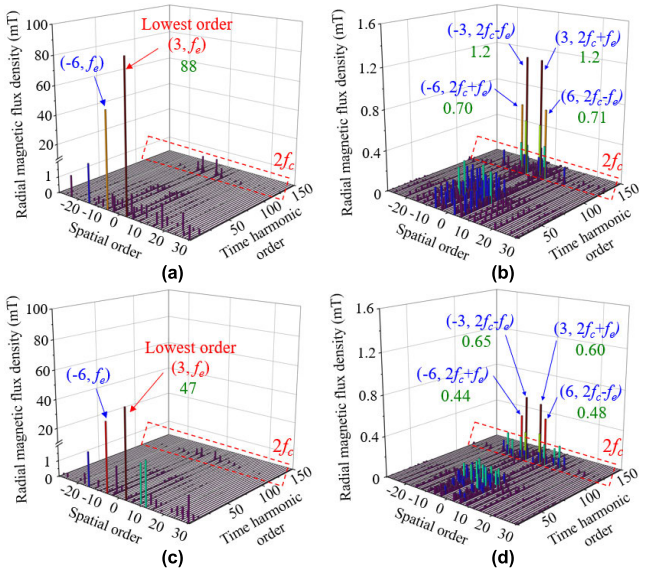


**FIGURE 9.** Radial magnetic flux density in air gap due to relative permeance and armature magnetomotive force. (a) Model A. (b) $f_c$ band of model A. (c) Model B. (d) $f_c$ band of model B.

The 6-pole 9-slot combination has the 3rd spatial harmonic in the armature at $f_e$. Model B has a lower radial magnetic flux density at the $f_e$ and $2f_c$ due to differences in average air gap length and pole shoe design. Also, the time harmonic order with the largest amplitude in the $2f_c$ domain is the same as the current harmonic order. According to the air gap magnetic flux density analysis results, model B is expected to have lower radial electromagnetic force density compared to model A.

Radial electromagnetic force is expressed as a function of time and spatial. By substituting (3)-(7) into (2), the radial force density can be expressed as (8), as shown at the bottom of the page.

As can be seen from (8), the radial electromagnetic force is divided into a total of six components according to their origin. A total of 6 components: PM field, armature reaction, interaction of PM field and armature reaction, and these three components multiplied by stator slotting. Table 3 shows the force order and frequency of the radial electromagnetic force depending on the source combination and shows the calculated results for the case of 6-pole and 9-slot. In general, the electromagnetic force is largest at $2f_e$, which is twice the fundamental frequency generated by the synthesis of the fundamental air gap magnetic flux density. The PM field has a 6th force order that is twice the pole pair. Except for the PM field, all source combinations occurred on the order of $6 \pm 9k$ at $2f_e$, where $k$ is a positive integer. Therefore, the force orders have …, -30, -21, -12, -3, 6, 15, 24, …. at $2f_e$. The force order is the spatial order of the radial force and has a great influence on the vibrational deformation of the stator.

**TABLE 3.** Force order and frequency of the radial electromagnetic force for source combinations and calculated 6-pole 9-slot values.

| Sources | Force order, 6Pole 9Slot | Frequency, 6Pole 9Slot |
|---|---|---|
| PM field | $p(\mu_1 \pm \mu_2)$, 6 (=2$p$) | $f_e(\mu_1 \pm \mu_2)$, $2f_e$ |
| Interaction of the PM field and stator slotting | $p(\mu_1 \pm \mu_2) \pm ks$, $6 \pm 9k$ | $f_e(\mu_1 \pm \mu_2)$, $2f_e$ |
| Armature reaction | $p(\nu_1 \pm \nu_2)$, $6 \pm 9k$ | $f_e(n_1 \pm n_2)$, $2f_e$ |
| Interaction of the armature reaction and stator slotting | $p(\nu_1 \pm \nu_2) \pm ks$, $6 \pm 9k$ | $f_e(n_1 \pm n_2)$, $2f_e$ |
| Interaction of the PM field and armature reaction | $p(\mu \pm \nu)$, $6 \pm 9k$ | $f_e(\mu \pm n)$, $2f_e$ |
| Interaction of the PM field, armature reaction, and stator slotting | $p(\mu \pm \nu) \pm ks$, $6 \pm 9k$ | $f_e(\mu \pm n)$, $2f_e$ |

**TABLE 4.** PWM harmonic frequency and force order at 2 $f_c$.

| Frequency domain | Current | Electromagnetic force | |
|---|---|---|---|
| | Time harmonic order | Time harmonic order | Force order |
| $2f_c$ | $2f_c \pm f_e$ | $2f_c$-$2f_e$ | -6(=-2$p$) $\pm 9k$ |
| | | $2f_c$ | 0 $\pm 9k$ |
| | | $2f_c$+$2f_e$ | 6(=2$p$) $\pm 9k$ |

Fig. 10 shows the stator deformation caused by the force order $r$ in the radial direction. The magnitude of the stator deformation for force orders $r = 0$ and force order $r \geq 2$ can be expressed as (9) and (10), respectively [27].

$$D_{r=0} = \frac{R_y R \cdot FM_{r=0}}{E \cdot T_y} \tag{9}$$

$$D_{r\geq 2} = \frac{12 R_y^3 R \cdot FM_{r\geq 2}}{E \cdot T_y^3 (r^2-1)^2} \tag{10}$$

$$\begin{aligned} P_r &= \frac{\mu_0}{2g^2}\left(\sum_{\mu=2k+1} F_\mu \cos(\mu p\omega_m t - \mu p\alpha + \theta_\mu)\right)^2 \times \left(\sum_n \sum_\nu F_\nu \cos(np\omega_m t - \nu p\alpha)\right)^2 \left(1 + \sum_k A_k \cos(ks\alpha)\right)^2 \\ &\approx \frac{\mu_0}{2g^2}\left[\begin{array}{l} \underbrace{F_{\mu 1}F_{\mu 2}\cos\{(\mu_1 \pm \mu_2)p\omega_m t - (\mu_1 \pm \mu_2)p\alpha + \theta_{\mu 1} \pm \theta_{\mu 2}\}}_{\text{PM field}} \\ \underbrace{+F_{\nu 1}F_{\nu 2}\cos\{(n_1 \pm n_2)np\omega_m t - (\nu_1 \pm \nu_2)p\alpha}_{\text{Armature reaction}} \\ \underbrace{+F_\mu F_\nu \cos(\mu \pm \nu)p\omega_m t - (\mu \pm \nu)p\alpha + \theta_\mu}_{\text{Interaction of the PM field and armature reaction}} \end{array}\right] \times \left[1 + \underbrace{2A_k \cos(ks\alpha)}_{\text{Stator slotting}}\right] \end{aligned} \tag{8}$$

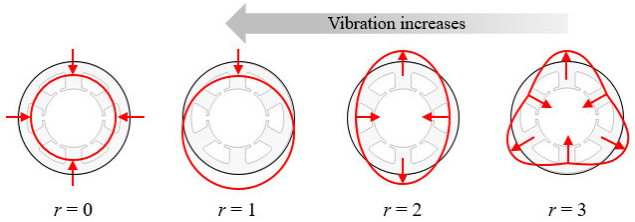


**FIGURE 10.** Deformation caused by radial forces with force order of 0, 1, 2, and 3.

Here, $R_y$, $R$, $T_y$, $E$, and $FM$ represent the yoke average radius, the inner radius of the stator, the yoke radial thickness, the Young's modulus, magnitude of the force, respectively. $FM_{r=0}$ represents the amplitude of the zero$^{th}$ order of the electromagnetic force, and $FM_{r\geq 2}$ represents the harmonic amplitude of the radial electromagnetic force order $r$. If the force order $r \geq 2$, then the deformation of the stator occurs almost in inverse proportion to the fourth power of the force order $r$. Thus, the radial vibration of the PMSM increases as the force order decreases, which implies that the lowest force order is the dominant source of the radial vibration. $R_y$, $R$, $T_y$, and $E$ of model A and model B compared in this paper were designed identically. Therefore, the noise and vibration of PMSM depend on the force order and magnitude of the electromagnetic force density.

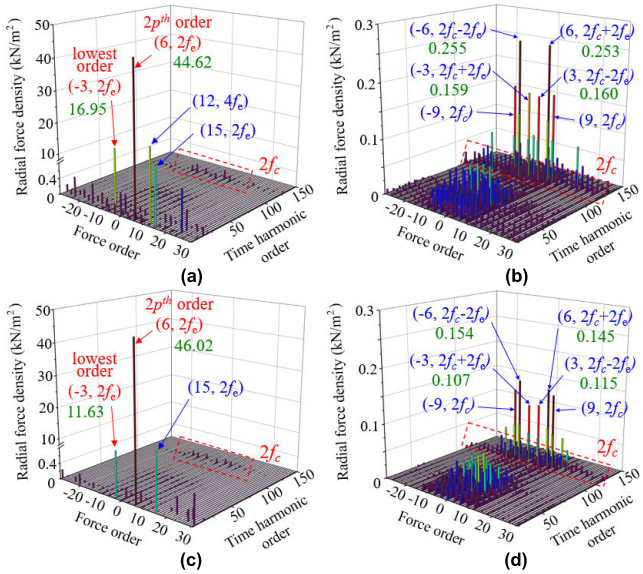


**FIGURE 11.** Radial electromagnetic force density. (a) Model A. (b) $f_c$ band of model A. (c) Model B. (d) $f_c$ band of model B.

2D electromagnetic FEA was performed to derive the radial electromagnetic force density, and the 2D FFT result is shown in Fig. 11. As expected, it has the largest amplitude at $2f_e$. The force orders of PM field sources and other sources have large amplitudes at 6$^{th}$ and $6 \pm 9k$. At $2f_e$, the lowest radial force order –3$^{rd}$ occurred, as expected in Table 3. As mentioned in Fig. 10, the smaller the force order, the greater the radial vibration of the PMSM, so the amplitude of the -3$^{rd}$ order force determines the vibration of the PMSM. At $2f_e$, amplitude of the –3$^{rd}$ force order of model B is 11.63 kN/m$^2$, which is much smaller than that of the model A with 16.95 kN/m$^2$. Similarly, in the carrier frequency band, near $2f_c$, the amplitude of the lowest order electromagnetic force of model B is smaller than that of model A. In particular, the 3$^{rd}$ force order occurred at the frequency of $2f_c$–$2f_e$, and the electromagnetic force amplitudes of model A and model B are 0.160 and 0.115 kN/m$^2$, respectively. In addition, the -3$^{rd}$ force order occurred at the frequency of $2f_c$+$2f_e$, and the electromagnetic force amplitudes of model A and model B are 0.159 and 0.107 kN/m$^2$, respectively. It was confirmed that the electromagnetic force of model B is much smaller than model A irrespective of the frequency. Regardless of the frequency range, the radial electromagnetic force density of model B was decreased compared to model A because, as explained earlier, the radial magnetic flux density of both the fundamental and harmonic components was decreased.

When analyzing the noise and vibration of PMSM, local tangential forces must also be considered. When a local tangential force is applied to the edge of the tooth, a lever arm effect occurs, which generates a force in the radial direction to cause vibration [28]. Using the Maxwell stress tensor method, the tangential force density can be obtained from the radial and tangential air gap flux densities.

$$P_t = \frac{B_r B_t}{\mu_0} \tag{11}$$

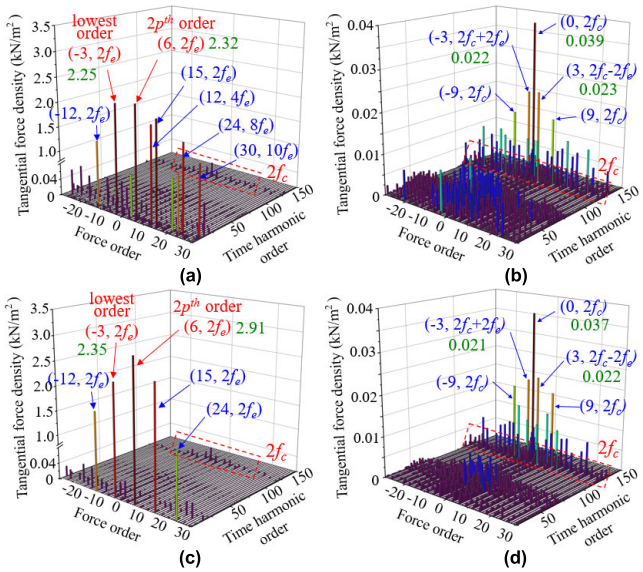


**FIGURE 12.** Tangential electromagnetic force density. (a) Model A. (b) $f_c$ band of model A. (c) Model B. (d) $f_c$ band of model B.

Fig. 12 shows the results of 2D FFT after performing 2D electromagnetic FEA on tangential electromagnetic force density. The tangential electromagnetic force density has a very small amplitude compared to the radial electromagnetic force density. Also, the amplitude of the 6$^{th}$ force order caused by the PM field is not large and is similar to other electromagnetic force densities. The tangential electromagnetic forces of model A and model B have similar

amplitudes in the $2f_c$ domain. Table 4 shows the PWM harmonic frequency of the input current, and the time harmonic and force order of the electromagnetic force. The carrier frequency sideband harmonics of the PWM current produce armature magnetic flux density harmonics in the air gap as shown in Fig. 9. The harmonics of the armature magnetic flux density combine with the PM field fundamental components to produce harmonics of the electromagnetic force density.

**TABLE 5. Maximum values of the electromagnetic force density for model A and model B.**

| Direction | Frequency | Force order $\lvert r \rvert$ | Electromagnetic force (kN/m$^2$) Model A | Model B | Ratio (B/A) |
|---|---|---|---|---|---|
| Radial | $2f_e$ | 3 | 16.95 | 11.63 | 69% |
| | $2f_c$ domain | 3 | 0.159 | 0.115 | 72% |
| Tangential | $2f_e$ | 3 | 2.25 | 2.35 | 104% |
| | $2f_c$ domain | 0 | 0.039 | 0.037 | 95% |
| | $2f_c$ domain | 3 | 0.023 | 0.022 | 96% |

Table 5 lists the maximum values of the radial and tangential electromagnetic force densities of the lowest force order in the $2f_e$ and $2f_c$ domain. 1st and 2nd of the force order $r$ do not occur, and under the condition of (10), the lowest order among the force orders $r \geq 2$ is $r = 3$. According to the results of the electromagnetic force analysis, the tangential electromagnetic force has a similar amplitude in both models, but the radial electromagnetic force has a larger amplitude in model A than model B. Therefore, it is expected that model A will have larger vibration than model B.

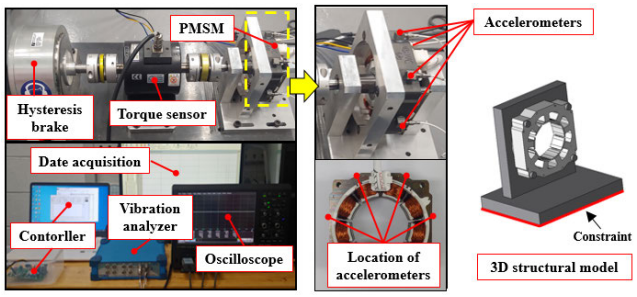


**FIGURE 13. Setup for the vibration test and 3D structural model.**

### D. NOISE AND VIBRATION ANALYSIS OF PMSM

In this section, the noise and vibration characteristics of the PMSM according to the electromagnetic force density are analyzed. The effect of electromagnetic force density on vibration of PMSM was analyzed by performing 3D FEA analysis and vibration test for model A and model B, respectively. Fig. 13 shows the vibration test environment and 3D structural model. The vibration test environment consists of hysteresis brake, torque sensor, PMSM, accelerometer, controller, data acquisition system, vibration analyzer, and oscilloscope. The accelerometer used was an 8776A50 from Kistler, and four accelerometers were mounted using adhesive to the PMSM surface. The sensitivity and acceleration range of the accelerometer are 100mV/g ±15% and ±50g, respectively. As a vibration analyzer, OR35 from OROS was used. Two accelerometers were mounted on the teeth of the stator and the others mounted on the yokes on either side of the stator. The test result used the average of 4 accelerometers. The vibration test was performed under the same conditions as the 2D snd 3D FEA: torque 0.23 Nm and electrical angular velocity 75 Hz. In the case of the 3D structural model, the same constraints were applied to the L-jig floor as in the vibration test.

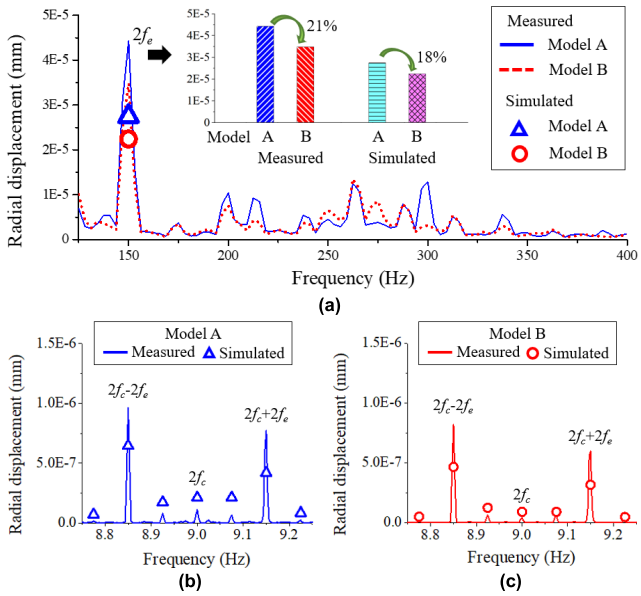


**FIGURE 14. Vibration test and 3D FEA results of PMSM.**

Fig. 14 shows the comparison between the 3D FEA results and the vibration test results for model A and model B. At $2f_e$ (=150 Hz), where the amplitude of the electromagnetic force is the largest, the vibration of PMSM occurred the largest. As expected, the vibration displacement of model B was lower than that of model A by 21% and 18%, respectively, in the experiment and 3D FEA. It can be seen that the vibration displacement of model B is lower than that of model A even in the $2f_c$ domain where electromagnetic force is generated significantly among high frequencies. Although the radial displacements of the simulated and measured results have errors, it can be tolerated since the trend that radial displacement of model B is lower than model A agrees well with the simulation results. The errors can potentially occur since the test system is much more complicated than the simulation environment, such as stacking structure of the stator and configuration of coil. However, all these factors are common to model A and model B, and the main difference of the two models is amplitude of the radial electromagnetic force. Therefore, it can be confirmed that the electromagnetic force affects the vibration displacement of the PMSM.

The vibration of the PMSM surface radiates noise, and the acoustic power can be predicted from the vibration velocity

and can be expressed as [29].

$$P_{acoustic\ power} = \frac{1}{2}\rho_0 c_0 u^2 dS\sigma \tag{12}$$

Here, $\rho_0$, $c_0$, $u$, $dS$, and $\sigma$ represent the density of the medium, the speed sound, the average of vibration velocity, the unit surface area, and radiation efficiency, respectively. Since acoustic power increases in proportion to the square of the vibration speed, the relatively high frequency domain is important. If models A and B are driven in the same environment, model B, which has a small vibration displacement in the $2f_c$ domain, is advantageous for noise.

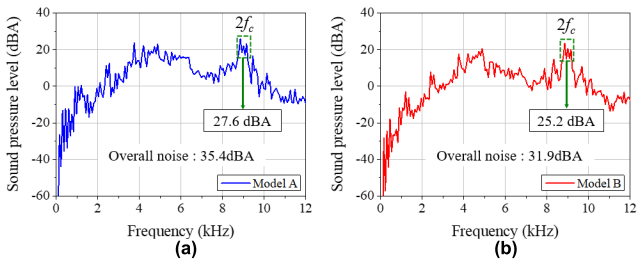


**FIGURE 15.** 3D FEA results of noise for PMSM. (a) Model A. (b) Model B.

Fig. 15 shows the noise 3D FEA results of model A and model B. Air is used as a medium around the motor, and at high frequencies, the electromagnetic force in the $2f_c$ domain is the largest, so the noise is also the highest. Both the overall noise level and the noise level in the $2f_c$ domain are lower in model B. 3D FEA analysis of noise was performed with a period of 75 Hz electrical angular velocity from 75 Hz to 12 kHz. The total noise was calculated as follows.

$$Overall\ noise = 10\log(10^{L_1/10} + 10^{L_2/10} + \cdots + 10^{L_n/10}) \tag{13}$$

The overall noise is calculated as the sum of the sound pressure levels, and $L_1$ and $L_2$ are the sound pressure levels at 75 Hz and 150 Hz, respectively. In summary, the $2f_e$ and $2f_c$ domain component of the electromagnetic force generated in PMSM greatly contributes to the vibration displacement and noise of PMSM, respectively. Therefore, the noise and vibration of PMSM can be reduced through electromagnetic design.

## III. NOISE AND VIBRATION OF COMPRESSOR

As shown in Fig. 1, the reciprocating compressor has a compression part and PMSM combined inside, and the combined body is supported by an elastic spring. Elastic spring and lower shell are connected, and refrigerant gas and lubricating oil are stored in the sealed shell. Refrigerant gas is compressed by the reciprocating motion of the compressor, and the source of noise/vibration generated when the compressor is operating can be divided into flow and structure. Also, since the compressor reciprocates through the PMSM, noise/vibration of the PMSM is also generated. This section analyzes the effect of noise/vibration of PMSM on noise/vibration of compressor.

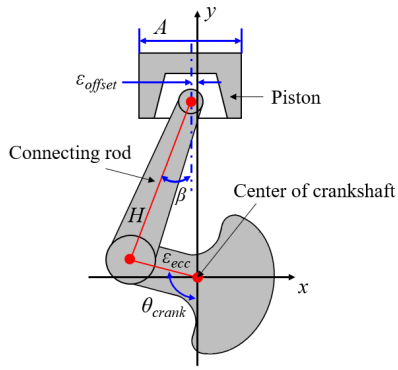


**FIGURE 16.** Schematic diagram of the reciprocating compressor.

### A. STRUCTURE AND COMPRESSION PROCESS OF RECIPROCATING COMPRESSOR

Fig. 16 shows the schematic diagram of the reciprocating compressor system, and the position of the crankshaft can be expressed as follows through the Cartesian coordinate system [30].

$$x_{crankshaft} = -\varepsilon_{ecc}\sin(\theta_{crank}) \tag{14}$$

$$y_{crankshaft} = -\varepsilon_{ecc}\cos(\theta_{crank}) \tag{15}$$

Here, $\varepsilon_{ecc}$ is the eccentricity of the crankshaft, $\theta_{crank}$ is the rotating angular of crankshaft, and the position of the piston can be expressed as follows [30].

$$x_{piston} = -\varepsilon_{offset} \tag{16}$$

$$y_{piston} = H\cos(\beta) - \varepsilon_{ecc}\cos(\theta_{crank}) \tag{17}$$

Here, $\varepsilon_{offset}$, $H$ and $\beta$ represent the offset of the center of the crankshaft and the center of the piston, the length of the connecting rod, and the tilt angle, respectively. The volume of the cylinder and the position of the piston have the following relationship [30].

$$V_{cylinder} = \frac{\pi A^2}{4}(y_{piston,\max} - y_{piston}) + V_0 \tag{18}$$

Here $A$ is the piston diameter and $V_0$ is the dead volume including the top clearance space of the cylinder shown in Fig. 17. Assuming that it is a polytropic compression process, the pressure inside the cylinder can be expressed as [30].

$$P_{cylinder}V_{cylinder}^{\gamma} = Const \tag{19}$$

Here, $P_{cylinder}$ and $\gamma$ are the pressure inside the cylinder and the polytropic index of the refrigerant gas, respectively. The compression process of the reciprocating compressor consists of four stages: compression, discharge, expansion, and suction, as shown in Fig. 17. First, as the piston moves from the bottom dead center (BDC) to the top dead center (TDC), the volume inside the cylinder decreases and the pressure increases. The refrigerant gas inside the cylinder is converted from a low-temperature/low-pressure state to a high-temperature/high-pressure state. Second, before the piston reaches TDC, the pressure inside the cylinder is higher than the pressure outside the cylinder, and the discharge valve opens to discharge high-temperature/high-pressure

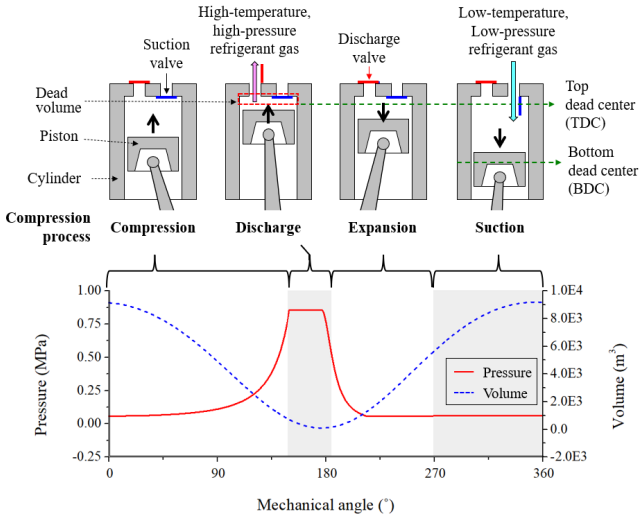


**FIGURE 17.** Volume and pressure change inside the cylinder according to the compression stroke process.

refrigerant gas. Also, a small amount of high-temperature and high-pressure refrigerant gas remains in the dead volume inside the cylinder. Third, when the piston moves from TDC to BDC, the high-temperature/high-pressure refrigerant gas remaining in the dead volume rapidly expands. Finally, when the pressure inside the cylinder is lower than the outside pressure, the suction valve opens and low-temperature/low-pressure refrigerant gas flows into the cylinder until the piston reaches the BDC point. The pressure inside the cylinder remains parallel at low pressure until compression begins.

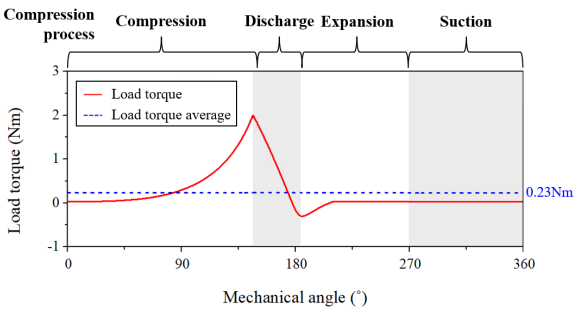


**FIGURE 18.** Load torque by refrigerant gas compression.

Fig. 18 shows the load torque due to refrigerant gas compression in a reciprocating compressor. The load torque can be expressed as.

$$T_{load} = \frac{P_{cylinder}\varepsilon_{ecc}\frac{\pi A^2}{4}\sin(\theta_{crank} - \beta)}{\cos(\beta)} \tag{20}$$

Like the pressure inside the cylinder, the load torque increases during compression and decreases when discharge begins. In the discharge section, the discharge valve opens before the piston reaches TDC, so the pressure remains constant and then decreases, but the load torque immediately decreases. The small negative peak in the load torque curve is caused by the expansion of the refrigerant gas inside the dead volume. The largest load torque occurs when the discharge valve opens during 1 cycle of the mechanical angle of the compressor. The load torque average is 0.23 Nm, which is about 11.5% of the peak load torque. That is, a very large peak load torque compared to the average load torque is generated in the compression process cycle.

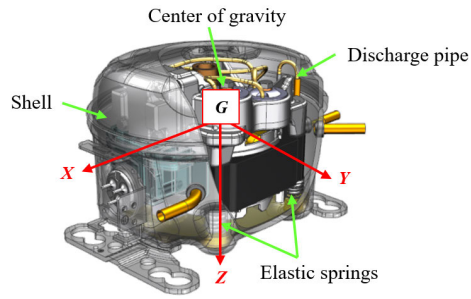


**FIGURE 19.** Reciprocating compressor support structure modeling and coordinates.

Fig. 19 shows the center of gravity G and the X, Y, Z coordinate system of the main body in the reciprocating compressor. The main body is a structure in which compression parts and PMSM are combined. Four elastic springs support the bottom of the main body, and a discharge pipe is connected to the shell on the side to support the main body. The equation of motion of a reciprocating compressor can be expressed as:

$$M\ddot{X} + C\dot{X} + KX = F \tag{21}$$

Here, $M$ is the mass matrix of the main body, $C$ and $K$ are the damping and stiffness matrices supported by the spring and discharge pipe, respectively. Also, $X$ is the vibration response, including translation and rotation motion, $F$ is the excitation force. The excitation force acting on the reciprocating compressor is generated by the rotational motion of the PMSM and the translational motion of the piston. Rotation and translation generate inertia forces that act on the main body. This inertial force changes the center of gravity of the main body, generates vibration of the main body, and is transmitted to the shell through four elastic springs and a discharge pipe. Therefore, the variable load generated during the compression process of the reciprocating compressor excites the main body and repeatedly vibrates according to the supporting characteristics of the main body mass, spring, and discharge pipe. Since the cycle of the compression process is equal to the mechanical angular velocity, the vibration cycle of the reciprocating compressor is also equal to the mechanical angular velocity. The reciprocating compressor used in refrigerators adjusts the mechanical angular velocity according to the required cooling capacity. In general, reciprocating compressors operated with variable speed operate at a mechanical angular velocity of 20-30 Hz when the temperature of the refrigerator is stable.

### B. EFFECT OF PMSM ON COMPRESSOR VIBRATION

Fig. 20(a) shows the manufactured reciprocating compressor. Model A and model B used the same mechanical parts

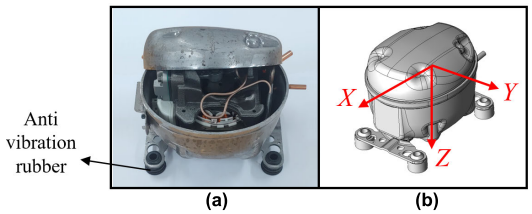


**FIGURE 20.** Environment of compressor vibration test. (a) Manufactured compressor. (b) Measurement coordinates.

and only the PMSM was replaced. Fig. 20(b) shows the coordinate system measured during compressor vibration test. The $X$, $Y$, and $Z$ coordinates represent the cylinder compression direction, the orthogonal direction to $X$, and the height direction, respectively. The vibration test of the compressor used the same acceleration sensor and measuring equipment as the vibration test of PMSM, and the test conditions complied with EN 12900 / CECOMAF standards. According to the CECOMAF standard, the suction and discharge pressures of the compressor were set to -0.43kg/cm$^2$G and 6.84 kg/cm$^2$G, respectively. Also, the compressor was placed on the test site using anti-vibration rubber.

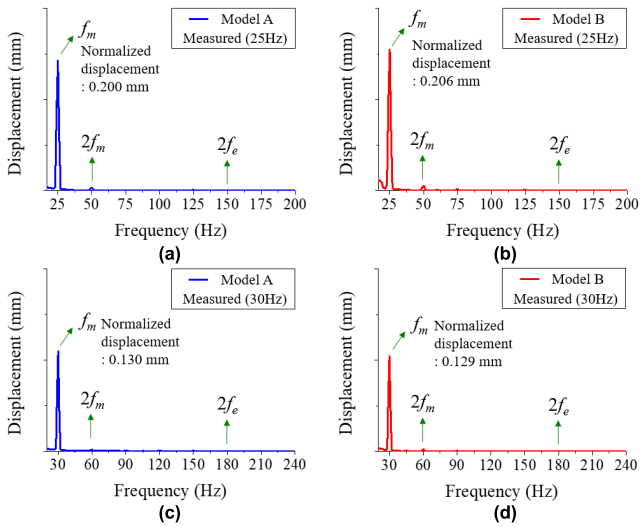


**FIGURE 21.** FFT results of Compressor Vibration Test. (a) Model A at 25Hz. (b) Model B at 25Hz. (c) Model A at 30Hz. (d) Model B at 30Hz.

Fig. 21 shows the FFT results of the vibration test of the compressor using model A and model B, and the vibration displacement is the sum of $X$, $Y$, and $Z$ coordinates. For security issue, the vibration displacement of the compressor is not indicated and the vibration displacement of model A at 25 Hz is normalized to 0.2 mm. Here, $f_m$ represents the mechanical angular velocity, and the compressor was operated at 25 Hz and 30 Hz, which are the main operating ranges of the refrigerator. The magnitude of the vibration displacement of the compressor is greatest at the mechanical angular velocity $f_m$ equal to the cycle of the compression process. Comparing model A and model B at $f_m$, the displacement of the compressor is similar at 25 Hz and 30 Hz. The magnitude of the displacement at $2f_e$, where the vibration of PMSM is the largest, is very small compared to $f_m$, where the vibration displacement of the compressor is the largest. For security issue purposes, the vibration displacement of the compressor is not indicated, but the vibration displacement at $f_m$ of the compressor is several thousand times larger than the vibration displacement at $2f_e$ of the PMSM. Through the vibration test of PMSM and compressor, it can be seen that the vibration displacement of the motor does not affect the vibration displacement of the compressor.

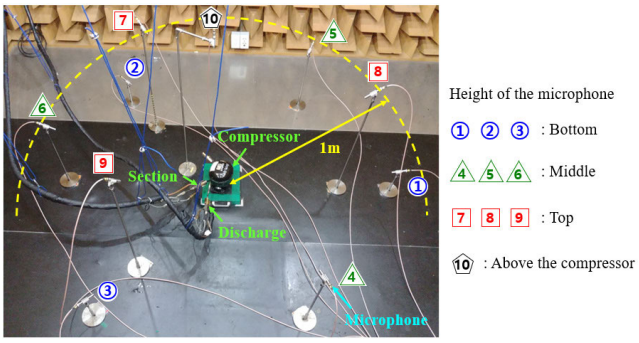


**FIGURE 22.** Environment of Noise Test for Compressor.

### C. EFFECT OF PMSM ON COMPRESSOR NOISE

This time, we analyze the relationship between PMSM and compressor noise. The compressor used for the noise analysis is the same as the one used for the vibration test. Fig. 22 shows the compressor noise test environment. The noise test was performed in a semi-anechoic room according to the regulations of ISO 3744: 2010, and the same EN 12900 /CECOMAF standard as the vibration evaluation was used for operating conditions. For noise measurement, a GRAS 46AE 1/2" CCP free-field standard microphone was used, and signal processing and data were collected using a Bruel & Kjaer_Type 3560B FFT analyzer. The frequency range, dynamic range and sensitivity of the microphone are 3.15 Hz to 20 kHz, 17 dBA to 138 dBA, and 50 mV/Pa, respectively. A total of ten microphones were installed, three each at the top, middle, and bottom heights, and one installed just above the compressor. The distance between the microphones and the compressor is 1m.

Fig. 23 compares the compressor sound pressure levels of model A and model B at mechanical angular velocities of 25 Hz and 30 Hz. For security issue, the sound pressure level of the compressor is not indicated, and the overall noise of model A at 25 Hz is normalized to 50.0 dBA. In the compressor state, the overall noise of model B is 1.0 dBA and 0.3 dBA lower than model A at 25 Hz and 30 Hz, respectively. Flow-induced noise and structure-induced noise, which are the noise sources of reciprocating compressors, occur below 1 kHz and between 3-5 kHz, respectively [30]. The electromagnetic noise of PMSM coexists with the noise factor of the compressor in the region below 5 kHz. For this reason, the noise difference in the compressor state is smaller than the noise difference expected in the PMSM state between model A and model

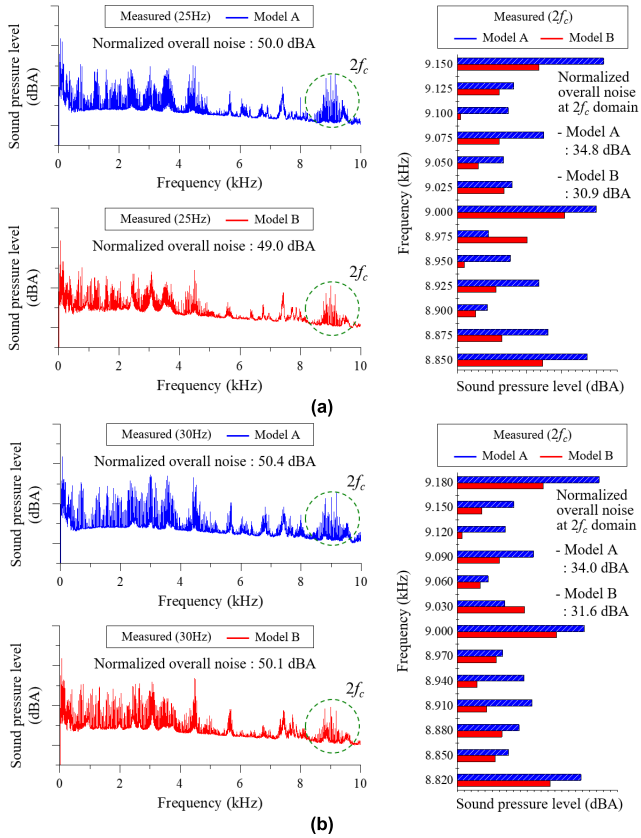


**FIGURE 23.** Normalized overall noise of the compressor for model A and model B. (a) 25Hz. (b) 30Hz.

B. In the region above 5 kHz, electromagnetic noise is the main cause. PMSM using the PWM method has large electromagnetic noise at the current ripple frequency. In both model A and model B, the electromagnetic noise of PMSM and compressor was generated significantly at the current ripple frequency of 9 kHz. Comparing the $2f_c$ domain where the noise effect of PMSM is dominant, model B is 3.9 dBA and 2.4 dBA lower than model A at 25 Hz and 30 Hz, respectively. This has similar values to the 3D FEA results of noise for PMSM, as expected earlier. Unlike vibration, the electromagnetic noise component of PMSM appears the same in the noise of the compressor. Generally, the flow-induced noise and structure-induced noise of reciprocating compressors are located below 5 kHz, so it is recommended to design the PWM current ripple frequency above 5 kHz so that it does not overlap with the compressor noise.

**TABLE 6.** Comparison of noise/vibration in PMSM and compressor of model A and model B.

| Type | Machinery / Frequency | Unit | $f_m$ (25Hz) Model A | $f_m$ (25Hz) Model B | Ratio (B/A) |
|---|---|---|---|---|---|
| Vibration | PMSM / $2f_e$ | mm | 4.4e-5 | 3.5e-5 | 79% |
| | Compressor / $f_m$ | | 0.200 | 0.206 | 103% |
| Noise | PMSM / $2f_c$ | dBA | 27.6 | 25.2 | 91% |
| | Compressor / $2f_c$ | | 34.8 | 30.9 | 89% |

Table 6 compares the noise/vibration results of model A and model B. Model B, which was designed to reduce electromagnetic force, showed a noise/vibration reduction effect of about 10-20% compared to model A, excluding the vibration of the compressor.

## IV. CONCLUSION

In this paper, the effect of PMSM's electromagnetic force on the noise and vibration of a reciprocating compressor for refrigerators was analyzed. First, for the purpose of comparative analysis, model B was designed so that the electromagnetic force is reduced compared to the base model A through optimization design. Then analyze the PWM current and compare the radial/tangential electromagnetic force between model A and model B. Compared to model A, model B has lowest-order radial electromagnetic force maxima of 69% and 72% at $2f_e$ and $2f_c$, respectively. Second, the effect of the electromagnetic force on the vibration/noise of the PMSM was analyzed. In PMSM, the maximum radial vibration displacement occurred at $2f_e$, and model B had a magnitude of 79% compared to model A. As for the PMSM noise generated the largest at $2f_c$, model B showed 91% of the sound pressure level compared to model A. Therefore, it was confirmed that the electromagnetic force has a close relationship with the noise/vibration of PMSM. Third, the effect of the electromagnetic force on the vibration/noise of the reciprocating compressor was analyzed. In the reciprocating compressor, the maximum vibration displacement occurred at $f_m$ and the magnitude of the two models was similar. Since the vibration displacement by the compression stroke of the reciprocating compressor is very large compared to the vibration displacement by PMSM, the electromagnetic force has no effect on the vibration characteristics of the compressor. As for the noise of the reciprocating compressor at $2f_c$, model B showed a sound pressure level of 89% compared to model A. Reducing the electromagnetic force of the PMSM reduces the noise in the reciprocating compressor, but does not affect the vibration displacement of the reciprocating compressor. Therefore, it is necessary to understand this correlation when designing a PMSM used in a reciprocating compressor.

## REFERENCES

[1] J. Y. Jeon, J. You, and H. Y. Chang, "Sound radiation and sound quality characteristics of refrigerator noise in real living environments," *Appl. Acoust.*, vol. 68, no. 10, pp. 1118–1134, Oct. 2007.

[2] J. Guo, J. Luo, Y. Guo, X. Pan, X. Fang, and X. Wu, "Noise test and control for household refrigerator compressor," in *Proc. IEEE Int. Conf. Inf. Autom.*, Aug. 2015, pp. 112–115.

[3] A. H. Sabry and P. J. Ker, "DC environment for a refrigerator with variable speed compressor; Power consumption profile and performance comparison," *IEEE Access*, vol. 8, pp. 147973–147982, 2020.

[4] K.-W. Lee, D.-K. Kim, B.-T. Kim, and B.-I. Kwon, "A novel starting method of the SPM-type BLDC motors without position sensor for reciprocating compressor," *IEEE Trans. Ind. Appl.*, vol. 44, no. 1, pp. 85–92, Jan./Feb. 2008.

[5] F. W. Yu and K. T. Chan, "Environmental performance and economic analysis of all-variable speed chiller systems with load-based speed control," *Appl. Thermal Eng.*, vol. 29, pp. 1721–1729, Jun. 2009.

[6] P. A. Lindahl, M. T. Ali, P. Armstrong, A. Aboulian, J. Donnal, L. Norford, and S. B. Leeb, "Nonintrusive load monitoring of variable speed drive cooling systems," *IEEE Access*, vol. 8, pp. 211451–211463, 2020.

[7] Z. Wu, Y. Fan, C. H. T. Lee, D. Gao, and K. Yu, "Vibration optimization of FSCW-IPM motor based on iron-core modification for electric vehicles," *IEEE Trans. Veh. Technol.*, vol. 69, no. 12, pp. 14834–14845, Dec. 2020.

[8] A. M. El-Refaie, "Fractional-slot concentrated-windings synchronous permanent magnet machines: Opportunities and challenges," *IEEE Trans. Ind. Electron.*, vol. 57, no. 1, pp. 107–121, Jan. 2010.

[9] T. Sun, J.-M. Kim, G.-H. Lee, J.-P. Hong, and M.-R. Choi, "Effect of pole and slot combination on noise and vibration in permanent magnet synchronous motor," *IEEE Trans. Magn.*, vol. 47, no. 5, pp. 1038–1041, May 2011.

[10] S. Zuo, F. Lin, and X. Wu, "Noise analysis, calculation, and reduction of external rotor permanent-magnet synchronous motor," *IEEE Trans. Ind. Electron.*, vol. 62, no. 10, pp. 6204–6212, Oct. 2015.

[11] Z. Wu, Y. Fan, H. Wen, and D. Gao, "Vibration suppression of FSCW-IPM with auxiliary slots," in *Proc. IEEE Energy Convers. Congr. Expo. (ECCE)*, Sep. 2018, pp. 3222–3227.

[12] F. Lin, S.-G. Zuo, W.-Z. Deng, and S.-L. Wu, "Reduction of vibration and acoustic noise in permanent magnet synchronous motor by optimizing magnetic forces," *J. Sound Vibrat.*, vol. 429, pp. 193–205, Sep. 2018.

[13] S. Das, A. Chowdhury, Z. Wan, M. B. Kouhshahi, A. P. Ortega, and Y. Sozer, "Sensitivity analysis based NVH performance evaluation in permanent magnet synchronous machines using lumped unit force response," in *Proc. IEEE Energy Convers. Congr. Expo. (ECCE)*, Oct. 2020, pp. 802–807.

[14] D. Kim, M. Park, J. Sim, and J. Hong, "Advanced method of selecting number of poles and slots for low-frequency vibration reduction of traction motor for elevator," *IEEE/ASME Trans. Mechatronics*, vol. 22, no. 4, pp. 1554–1562, Aug. 2017.

[15] F. Lin, S. Zuo, W. Deng, and S. Wu, "Modeling and analysis of electromagnetic force, vibration, and noise in permanent-magnet synchronous motor considering current harmonics," *IEEE Trans. Ind. Electron.*, vol. 63, no. 12, pp. 7455–7466, Dec. 2016.

[16] R. Islam and I. Husain, "Analytical model for predicting noise and vibration in permanent-magnet synchronous motors," *IEEE Trans. Ind. Appl.*, vol. 46, no. 6, pp. 2346–2354, Nov. 2010.

[17] A. J. Piña Ortega and L. Xu, "Investigation of effects of asymmetries on the performance of permanent magnet synchronous machines," *IEEE Trans. Energy Convers.*, vol. 32, no. 3, pp. 1002–1011, Sep. 2017, doi: 10.1109/TEC.2017.2684165.

[18] R. M. Pindoriya, B. S. Rajpurohit, and R. Kumar, "A novel application of harmonics spread spectrum technique for acoustic noise and vibration reduction of PMSM drive," *IEEE Access*, vol. 8, pp. 103273–103284, 2020.

[19] T. Hara, T. Ajima, K. Hoshino, and A. Ashida, "Carrier electromagnetic vibration of DC voltage fluctuation in permanent-magnet synchronous motor with distributed winding," *IEEE Trans. Ind. Appl.*, vol. 56, no. 5, pp. 4623–4631, Sep. 2020.

[20] J. Xu and H. Zhang, "Random asymmetric carrier PWM method for PMSM vibration reduction," *IEEE Access*, vol. 8, pp. 109411–109420, 2020.

[21] O. A. Mohammed, A. A. Khan, A. M. El-Tallawy, A. Nejadpak, and M. J. Roberts, "A wavelet filtering scheme for noise and vibration reduction in high-frequency signal injection-based sensorless control of PMSM at low speed," *IEEE Trans. Energy Convers.*, vol. 27, no. 2, pp. 250–260, Jun. 2012.

[22] M. Bertoluzzo, G. Buja, R. K. Keshri, and R. Menis, "Sinusoidal versus square-wave current supply of PM brushless DC drives: A convenience analysis," *IEEE Trans. Ind. Electron.*, vol. 62, no. 12, pp. 7339–7349, Dec. 2015.

[23] K. Lee, S. Park, and S. Jeong, "A seamless transition control of sensorless PMSM compressor drives for improving efficiency based on a dual-mode operation," *IEEE Trans. Power Electron.*, vol. 30, no. 3, pp. 1446–1456, Mar. 2015.

[24] S. Kim, S. Lee, J. Kim, T. H. Lee, and M. Lim, "Robust design optimization of surface-mounted permanent magnet synchronous motor using uncertainty characterization by bootstrap method," *IEEE Trans. Energy Convers.*, vol. 35, no. 4, pp. 2056–2065, Dec. 2020.

[25] S. Im, S. Lee, D. Kim, G. Xu, S. Shin, and M. Lim, "Kriging surrogate model-based design of an ultra-high-speed surface-mounted permanent-magnet synchronous motor considering stator iron loss and rotor eddy current loss," *IEEE Trans. Magn.*, vol. 58, no. 2, pp. 1–5, Feb. 2022.

[26] D. G. Holmes and T. A. Lipo, *Pulse Width Modulation for Power Converters: Principles and Practice*. Hoboken, NJ, USA: Wiley, 2003.

[27] S. Wang, J. Hong, Y. Sun, and H. Cao, "Analysis of zeroth-mode slot frequency vibration of integer slot permanent-magnet synchronous motors," *IEEE Trans. Ind. Electron.*, vol. 67, no. 4, pp. 2954–2964, Apr. 2020.

[28] H. Lan, J. Zou, Y. Xu, and M. Liu, "Effect of local tangential force on vibration performance in fractional-slot concentrated winding permanent magnet synchronous machines," *IEEE Trans. Energy Convers.*, vol. 34, no. 2, pp. 1082–1093, Jun. 2019.

[29] L. E. Kinsler, A. R. Frey, A. B. Coppens, and J. V. Sanders, *Fundamentals of Acoustics*, 4th ed. New York, NY, USA: Wiley, 2000.

[30] Y. Son, J. Choi, and S. Lee, "Noise source identification of the hermetic reciprocating compressor for refrigerator," *J. Mech. Sci. Technol.*, vol. 35, no. 11, pp. 4849–4858, Nov. 2021.

**CHI-SUNG PARK** received the master's degree in electrical engineering from Pusan National University, Pusan, South Korea, in 2011. He is currently pursuing the Ph.D. degree in automotive engineering with Hanyang University, Seoul, South Korea.

Since 2010, he has been with LG Electronics, Changwon, South Korea, where he is currently a Senior Research Engineer. His research interests include design and the analysis of vibration and noise of electric machines.

**JAE-HYUN KIM** received the bachelor's degree in mechanical engineering from Hanyang University, Seoul, South Korea, in 2017, where he is currently pursuing the Ph.D. degree in automotive engineering.

His research interests include design and the analysis of vibration and noise of electric machines.

**SOO-HWAN PARK** received the bachelor's degree in mechanical engineering and the Ph.D. degree in automotive engineering from Hanyang University, Seoul, Republic of Korea, in 2014 and 2022, respectively.

From 2019 to 2020, he was with the Korea Institute of Industrial Technology, Republic of Korea. Since 2022, he has been with the Research and Development Division, Hyundai Motor Company, Republic of Korea, where he is currently a Senior Research Engineer. His research interests include electromagnetic field analysis, design, the optimization of electric machines for automotive and robotics applications, and thermal management system for electric vehicles.

**MYUNG-SEOP LIM** (Member, IEEE) received the bachelor's degree in mechanical engineering and the master's and Ph.D. degrees in automotive engineering from Hanyang University, Seoul, South Korea, in 2012, 2014, and 2017, respectively.

From 2017 to 2018, he was a Research Engineer with Hyundai Mobis, Yongin, South Korea. From 2018 to 2019, he was an Assistant Professor with Yeungnam University, Daegu, South Korea. Since 2019, he has been with Hanyang University, where he is currently an Assistant Professor. His research interests include electromagnetic field analysis and electric machinery for mechatronics systems, such as automotive and robot applications.